Investigating the interaction of hydraulic fracture with pre-existing joints based on lattice spring modeling

Investigating the interaction of hydraulic fracture with pre-existing joints based on lattice spring modelling

Kaikai Zhao[a,b], Doug Stead[c], Hongpu Kang[a,b], Branko Damjanac[d], Davide Donati[c], Fuqiang Gao[a,b,*]

[a] State Key Laboratory of Coal Mining and Clean Utilization (China Coal Research Institute), Beijing, China

[b] Mining & Designing Branch, China Coal Research Institute, Beijing, China

[c] Engineering Geology and Resource Geotechnics, Simon Fraser University, Burnaby, BC, Canada [d] Itasca Consulting Group, Inc., Minneapolis, MN, United States

* Corresponding author: fuqgao@gmail.com (F. Gao).

Abstract

Pre-existing joints have a significant influence on the geometry of the fracture network induced by hydraulic fracturing. Understanding the interaction between hydraulic fractures (HF) and pre-existing joints is of great importance to optimize the design of hydraulic fracturing operations in many applications. A three-dimensional hydro-mechanical coupled lattice-spring code was employed to investigate the interaction mechanisms under different pre-existing fracture shear strength (cohesion and friction angle), in-situ stress, angle of approach, and varying treatment parameters (fluid viscosity and injection rate). Simulation results indicate that hydraulic fractures tend to cross pre-existing joints for high magnitudes of assumed of fracture cohesion, friction angle, stress difference, approach angle, fluid viscosity, and injection rate. Three basic model hydraulic fracture-joint relationships were noted which were termed zero-joint crossing, 1-joint crossing and 2-joint crossing. For varied assumed shear strength, in-situ stress, approach angle and treatment parameters, the contribution of tensilefailure in intact rock and shear-failure on pre-existing joints tends to be enhanced or reduced, which controls the dominant observed interaction behavior (slip or crossing) as well as the variation in the resulting stimulated reservoir area.

Keywords: Hydraulic fracturing, lattice spring modelling, Pre-existing joint, Hydro-mechanical coupling Interaction mechanism, Stimulated reservoir area

1. Introduction

Hydraulic fracturing has been extensively used as a stimulation technique to enhance the productivity in unconventional oil and gas reservoirs and in enhanced geothermal systems [1–5]. More recently hydraulic fracturing has been increasingly used in preconditioning operations in block caving mines and in the destressing of underground excavation [6,7]. The effectiveness of hydraulic fracturing stimulation in fractured formations are greatly affected by the interaction between the hydraulic fracture (HF) and the pre-existing joints. Moreover, for different joint mechanical properties, joint orientation, in-situ stress and treatment parameters, the HF propagation pathway can vary significantly. It is important to investigate the nature of fluid-driven fracturing

processes and in particular the interaction between joints and HF to improve the hydraulic fracturing design and control the resulting fracture network geometry.

Several authors investigated the factors influencing the hydraulic fracturing process, including the characteristics of the pre-existing joints, the in-situ stress state, the fracturing fluid viscosity and injection rate, and the anisotropy and heterogeneity of the rock mass [8–10]. Blanton [8] and Warpinski et al. [9] argued that the differences in the in-situ stress and the approach angle (i.e., the angle between the propagating HF and the joint) are the key factors determining HF propagation behavior in fractured formation. HF tend to cross pre-existing joints under high horizontal/vertical stress difference and high approach angle. In addition, an increase in injection rate or fluid viscosity will promote HF crossing the pre-existing fractures and reduce the fracture plane tortuosity [10]. Zhou et al. [11,12] performed a series of experiments to investigate the interaction between HF and pre-existing joints. Three fracture propagation conditions were noted: arrest of the HF, dilation of the joint, and crossing of the joint by the HF. These conditions were noted to depend on the shear strength of the joints, the approach angle, and in-situ differential stress. Daneshy [13] and Lamont and Jessen [14] argued that the HF crosses the pre-existing joints without change of original direction, but may be propagates along the joint plane in addition to dilation of joint. Liu et al. [15] proposed that HF propagates along the preferential fracture plane or the path of least resistance.

Numerous criteria have been established to predict the dominant mode of interaction behavior under certain simplifying assumptions. Renshaw and Pollard [16] proposed a crossing criterion for the interaction between a propagating fracture and a pre-existing joint at orthogonal intersection. Their criterion was extended by Gu et al. [17] to non-orthogonal hydraulic fracture-joint intersection. Sarmadivaleh and Rasouli [18] further expanded the application of Renshaw and Pollard's criteria to a cohesive interface with a non-orthogonal angle of approach, considering the cohesion and adhesion of the interface plane, and the sliding along the pre-existing joint. Blanton [19] proposed a model to investigate fracture re-initiation along a partially opened joint under a simplified shear stress distribution, assuming re-initiation would occur only in the sliding zone. The stress induced by the hydraulic fracture itself was not considered. As reported by Warpinski and Teufel [20] and Yao et al. [21], the stress field induced by the propagating hydraulic fracture is conducive for reducing the probability of arrest. However, they do not take into account the influence of injection rate and fluid viscosity on the crossing behaviors. In fact, field and laboratory experiments indicated that injection rate and fluid viscosity are key factors controlling the dominate interaction mode [10,22]. Chuprakov et al. [23] developed a multi-parameter Open-T model to take into account fluid injection parameters such as injection rate and fluid viscosity, but was restricted to the analysis of interaction behavior after an HF intersected a joint. Llanos et al. [24] proposed a simplified form of Renshaw and Pollard's criterion, which assumed a uniform pressure distribution in a HF. Zhao et al. [25] proposed a criterion for a toughness-dominated HF crossing a frictional interface by coupling the fluid flow and solid elastic deformation of the HF prior to intersecting with the frictional interface.

In laboratory experiment, it is difficult to quantitatively control the process of hydraulic fracture initiation and propagation, or to evaluate the influence of the pre-existing joint cohesive and frictional strength and the change in the fluid pressure field. Additionally, most of the simplified equations does not include the coupling of fluid flow and rock deformation. Therefore, extensive numerical models have been proposed to investigate

hydraulic fracture propagation. Wu and Olson [26] presented a simplified 3D approach providing solutions for the non-planar vertical fractures, based on the displacement discontinuity method (DDM). Kresse et al. [27] reported an unconventional fracture model (UFM) to simulate HF propagation in natural fracture network. Yamamoto et al. [28] described a 3D fracture propagation model based on the finite element method (FEM). Dahi-Taleghani and Olson [29] adopted the extended FEM (XFEM) to investigate the multistrandedhydraulic-fracture propagation, involving the interaction behavior between induced and natural fractures. Guo et al. [30] utilized the cohesive zone method (CZM) to investigate the intersection behavior between hydraulic fracture and interfaces under the condition that the propagation path of the HF was predefined. As reported by Yan et al. [31–34], both 2D and 3D fully coupled model with real pore seepage have been proposed for simulating hydraulic fracturing based on the finite-discrete element method (FDEM). The distinct element method (DEM), originally developed by Cundall [35] has been extensively used for varied applications in mining and civil engineering (e.g. rock slopes, underground excavations) for the solution of problems involving deformation, damage, fracturing, and stability of the fractured rock masses [36–38]. In the DEM, the fracture propagation pathway is modeled through the opening of contacts between blocks (e.g., using Voronoi or Trigon tesselation) [39], therefore the fracture trajectory is restricted to the prebuilt geometry of the contacts [40]. To overcome this limitation, Mas Ivars et al. [41] developed the synthetic rock mass (SRM) approach, which used the bonded particle model to represent intact material and the smooth joint model (SJM) to represent the preexisting joints. The SRM scheme has been originally implemented in the particle flow codes, PFC2D and PFC3D [42,43]. Recently, a lattice scheme code, XSite, has been developed by implementing the SRM approach, which is capable of modelling the propagation of tensilefracture in intact rock as well as slip and opening/closing of joint elements, and is computationally more efficient than PFC2D/3D models [44,45]. Xing et al. [46] used XSite to investigate hydraulic fracture containment, which considered the influence of the horizontal weak interfaces, stresses state, and material fracture toughness. Bakhshi et al. [47] adopted lattice modeling to simulate the interaction of hydraulic fracture and the natural interface considering the shear strength and stress anisotropy of the intact material. Fu et al. [48] used XSite to investigate the interaction between hydraulic fracture and nature fractures with spatially-varied mechanical and geometrical properties.

In this paper, we investigate the interaction behaviors between HF and pre-existing joints, and the corresponding fracture evolution process using the lattice scheme code XSite. Six sets of simulations are performed to examine the influence of the joint mechanical properties (cohesion and friction angle), the in-situ stress difference or deviatoric stress ($\Delta\sigma = \sigma_z - \sigma_x$), the approach angle, and the treatment parameters (fluid viscosity and injection rate). In order to quantitatively evaluate the performance of the hydraulic fracturing, the concept of stimulated reservoir area (SRA) is used. The shear-SRA is defined as the area of natural (i.e., pre-existing) joints that have experienced shear-slip, whereas the tensile-SRA is defined as the area of induced tensile-fracture in the rock matrix (i.e., area of HF).

2. Lattice modeling method

The code XSite allows for the investigation of SRM, through the incorporation of a discrete fracture network (DFN) within the latticespring simulating the intact material; the fracturing of the intact rock takes place through

spring breakage. The pre-existing joints are modeled using a SJM, approach [49]. XSite can simulate the interaction between the HF and pre-existing joints without restricting the trajectory of the fractures or HF-Joint interaction conditions. Pathway for fracture propagation results from the combination of intact-rock failure in tension and slip and dilation of pre-existing joints. The calibration factors that relate the strength and stiffness of springs to the macroscopic strength and elastic moduli of rock are a function of arrangement of the nodes, which is the same irrespective of the model resolution. Thus, these calibration factors can be calibrated and built into the lattice codes, avoiding the calibration step (more details about the macromicro parameter relation can be found in reference [45]). Verification of HF propagation in a viscosity-dominated regime and storage-toughness dominated regime has been presented by Damjanac and Cundall [45] and Fu et al. [48] respectively.

2.1. Mechanical model

As depicted in Fig. 1a, the lattice consists of a number of quasirandomly distributed discrete point masses (or lattice nodes) connected by springs to represent the rock matrix and joints. The DFN is overlaid on the lattice spring network and the springs intersected by the discontinuities are assigned the elastic and strength parameters of the fracture. If the two nodes of a spring are placed on the opposite sides of a joint plane, the spring will obey the SJM approach. The orientation of the discontinuity plane is considered during the analysis, disregarding the orientation of the single springs along the joint. Where joint planes cut springs, the angle of the plane is respected (not the spring orientation). Thus, shear and normal compliances for the joint are used instead [45,48].

The law of motion for translational degrees of freedom consists of the following central difference formulae for each node [45]:

$$\dot{u}_i^{(t+\Delta t/2)} = \dot{u}_i^{(t-\Delta t/2)} + \sum F_i^{(t)} \Delta t/m \qquad (1)$$

$$u_i^{(t+\Delta t)} = u_i^{(t)} + \dot{u}_i^{(t+\Delta t/2)} \Delta t \qquad (2)$$

where $u_i^{(t)}$ and $u_i^{(t)}$ are the velocity and position of component i(i = 1, 3) at time t. $\sum F_i^{(t)}$ is the sum of all the force-components acting on the node of mass *m*, with time step Δt. The angular velocities (ω_i) are calculated based on the central difference formula of angular momentum balance:

$$\omega_i^{(t+\Delta t/2)} = \omega_i^{(t-\Delta t/2)} + \frac{\sum M_i^{(t)}}{I} \Delta t \qquad (3)$$

where $M_i^{(t)}$ is the sum of all moment-components acting on the node of moment of inertia *I*.

The force change in the spring are calculated by the the relative displacements of thenodes:

$$F^N \leftarrow F^N + \dot{u}^N k^N \Delta t \qquad (4)$$

$$F_i^S \leftarrow F_i^S + \dot{u}_i^S k^S \Delta t \qquad (5)$$

where "N" denotes "normal", "*S*" denotes "shear", k^N and k^S are the spring normal and shear stiffnesses, respectively, and *F* is the spring force.

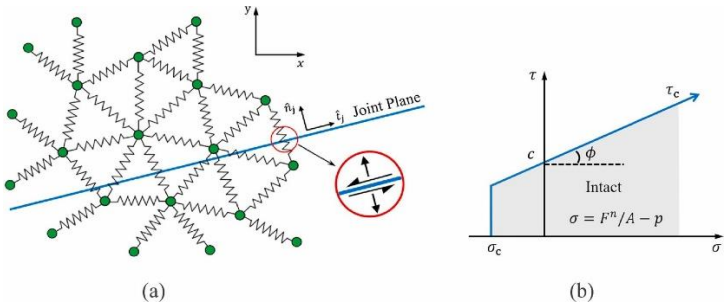

Fig. 1. Mechanical model: (a) schematic of a lattice array, with the implementation of a smooth joint. Note that the shear and normal parameters are considered, regardless the orientation of the intersected springs. Modified from [50]; (b) Spring strength envelope. Modified from [43].

The springs that obey the SJM do not act in the direction of the line connecting the nodes. Instead, they respect the direction of the joint plane that intersects the spring, thus, sliding on joint planes is independent of the local orientations of springs. Slip and opening of joint elements following the relations [50]:

If $F^n - pA < 0, \quad \text{then} \quad F^n = 0, \; F_i^s = 0;$

Else $F_i^s \Leftarrow \frac{F_i^s}{|F_i^s|}\min\{(F^n - pA)\tan\phi, |F_i^s|\}$ (6)

where F^n is the normal force, F_i^s is the shear force vector, p is the fluid pressure, A is the apparent area of the joint segment, and ϕ is the friction angle.

As illustrated in Fig. 1b, for the bonded joint, the joint status is updated based on the following relationships:

If $F^n - pA + \sigma_c A < 0$ or $|F_i^s| > \tau_c A$, joint condition follows Eq. (6); else, $F_i^s F_i^s$.

2.2. Flow model

As depicted in Fig. 2, the pipes are placed between the fluid elements (i.e. locations of either broken springs or springs that represent pre-existing joints). Fluid flow occurs through a network of pipes that connect fluid elements. By connecting newly formed microcracks to the existing network, the pipe network is updated automatically [49].

The lubrication equation is employed to calculate the fluid flow within a pipe. The flow rate along the pipe from fluid node "A" to node "B" is calculated as [41]:

$$q = \beta k_r \frac{a^3}{12\mu_f}[p^A - p^B + \rho_w g(z^A - z^B)] \qquad (7)$$

where a is aperture, μ_f is fluid viscosity, p^A and p^B are fluid pressures at nodes "A" and "B", respectively, z^A and z^B are elevations of nodes "A" and "B" respectively, ρ_w is fluid density, and g is the acceleration due to gravity. k_r is the relative permeability. Dimensionless parameter β is a calibration parameter used to match conductivity of a pipe network to the conductivity of a joint represented by parallel plates with aperture a. The parameter β can be determined as a function of the resolution and connectivity of the pipe network. The calibrated relation between β and the resolution is built into the code [49].

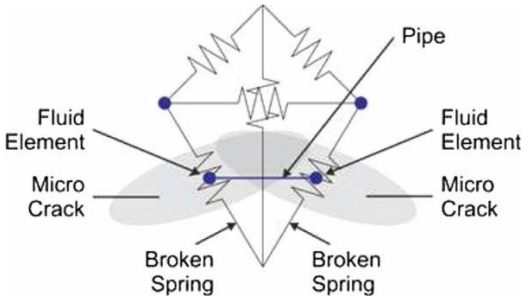

Fig. 2. Schematic diagram of the pipe network [49].

2.3. Hydro-mechanical coupling

Fluid flow is implemented in the pre-existing and stress-induced fractures which is fully coupled with mechanical deformation. Fluid pressure act as loading on the solid model, affecting both deformation and the strength of the solid model. Meanwhile, the deformation of the solid model causes pore pressure and aperture changes. Fracture permeability depends on aperture, or on the deformation of the solid model [49].

Although the initial equilibrium can be achieved running the model in fully coupled mode, it is much more computationally efficient to do it in uncoupled mode conducting mechanical calculation only. For initial states transient responses governed by coupled processes are not relevant because mechanical and flow models are typically in equilibrium and steady states. For that reason, the code can be run in three different modes: 1) fully coupled, 2) mechanical-only calculation, and 3) flow-only calculation.

2.4. Model setup

Fig. 3 shows the model setup; the dimensions of the investigated rock mass volume are 4 m × 4 m × 4 m. Two square, symmetrical, horizontal joints are incorporated, with dimension 3.7 m × 3.7 m and a spacing of 1 m. In order to initiate the hydraulic fracture propagation, an incipient joint, with a radius of 0.2 m, is placed at the centre of the model, perpendicular to the x-axis. The horizontal stress is assumed to be $\sigma_x = \sigma_y = 5$ MPa for all models, while varied σ_z values are used to analyze the role of the deviatoric stress. The initial joint aperture is assumed to be 0.1 mm. The simulation is initially run in the mechanical mode for 0.1 s (numerical time) to achieve the initial model equilibrium. Simulation continues in the hydro-mechanical coupling mode, as fluid is injected into the incipient joint at a constant rate. The mechanical and hydraulic parameters are listed in Table 1.

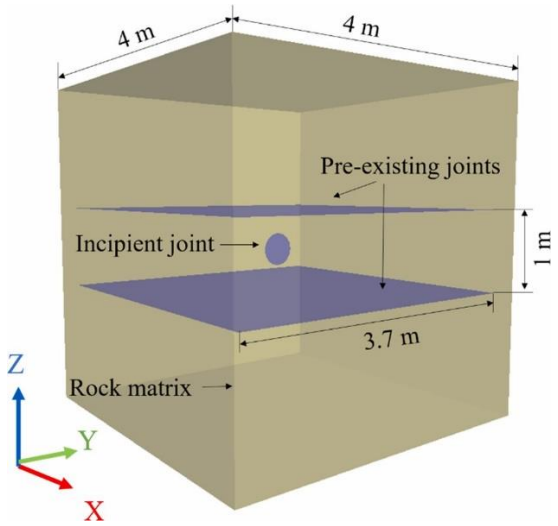

Fig. 3. Numerical model setup in XSite.

Table 1
Mechanical and hydraulic model input parameters.

Categories	Variables	Values
Joint properties	Joint cohesion, c (MPa)	0.3, 0.6 ,0.9, 1.2, 1.5
Stress state	Joint friction angle, φ (°)	25, 30, 35, 40, 45
	Approach angle, θ (°)	70, 75, 80, 85, 90
	Stress difference, Δσ (MPa)	2, 4, 6, 8, 10
Treatment parameters	Fluid viscosity, μ (mPa·s)	1, 3, 5, 7, 9
	Injection rate, Q (m^3/s)	0.0025, 0.003, 0.0035, 0.004, 0.0045
Intact rock	Young's modulus, E (GPa)	11.74
	Poisson's ratio, ν	0.221
	Tensile strength, σ_t (MPa)	7.5
	UCS, σ_c (MPa)	75

3. Model Results

3.1. Set 1: Effect of cohesion of pre-existing joints

For set 1, five models were simulated using a joint cohesion of 0.3, 0.6, 0.9, 1.2, and 1.5 MPa, respectively. Other parameters are listed as follows: ($\varphi = 30°$; $\sigma_z = 12.5$ MPa; $\theta = 90°$; $\mu = 1$ mPa·s; $Q = 0.003$ m^3/s). As shown in Fig. 4, three different simulated behaviors (with respect to the relationship between the HF and the pre-existing joints) were observed: zero-joint crossing HF, (for c = 0.3 MPa), 1-joint crossing, HF (for c = 0.6 MPa) and 2-joint crossing HF (for c = 0.9, 1.2 and 1.5 MPa).

As shown in Fig. 5a, an increase of the joint cohesion from 0.3 MPa to 0.9 MPa cause a marked decrease in shear-stimulated reservoir area, SRA, (from 11.39 m^2 to 9.30 m^2). Conversely, a negligible change (from 9.30 m^2 to 9.22 m^2) is noted when joint cohesion changes from 0.9 MPa to 1.5 MPa.

Fig. 5b shows the evolution of shear-SRA versus time for different cohesion values. The shear-SRA increased at a high rate in the period of 0.15 s to 0.4 s, reaching an inflection point at about 0.4 s, followed by a moderate

rate increase (0.4 s to 4.1 s). In general, the five curves overlap in the first stage of the simulation, before separating after about 0.4 s. Greater cohesion values will progressively generate lower shearSRA values towards the end of the simulation, compared to lower cohesion values. Curves for c = 0.3 MPa and 0.6 MPa show a similar pattern, characterized by a constant increase in cumulative shear-SRA. Curves for c = 0.9 MPa, 1.2 MPa, and 1.5 MPa, conversely, display a decrease in shear-SRA rate starting after about 3 s.

3.2. Set 2: Effect of joint friction angle

For set 2, five models were conducted with assumed joint friction angles of 25°, 30°, 35°, 40°, and 45°. Other parameters are listed as follows: (c = 0.6 MPa; σ_z = 12.5 MPa; θ = 90°; μ = 1 mPa·s; Q = 0.003 m^3/s). As shown in Fig. 6, different model results were observed after 4.1 s simulation time: zero- joint crossing (φ = 25°), 1joint crossing (φ = 30°) and 2-joint crossing (φ = 35°, 40°, and 45°). The simulation results show that an increase in assumed joint friction angle cause the HF to cross both joints.

Fig. 7a indicates that there is a marked decrease in shear-SRA with the increase in the assumed joint friction angle from 25° to 35°, followed by a negligible change over the range of joint friction between 35° and 45°. As the assumed joint friction angle is increased from 25° to 35°, the shear-SRA decreased by 1.78 m^2 (from 11.08 m^2 to 9.30 m^2). With increase in the assumed joint friction angle from 35° to 45°, the shear-SRA decreased by 0.09 m^2 (from 9.30 m^2 to 9.21 m^2).

Fig. 7b shows the evolution of the shear-SRA with simulation time for different assumed joint friction angle. In general, the greater the assumed joint friction angle, the lower the shear-SRA curve. The shearSRA increases rapidly over the simulation period of 0.15 s to 0.4 s, with a marked change in gradient at 0.4 s, followed by constant lower gradient between 0.4 s and 4.1 s. In the early stage, the five curves overlap, while at the later stage of simulation they deviate. The shear-SRA graphs for φ = 25° and 30° display a similar trend, with a constant increase after 0.4 s, while for φ = 35°, 40°, and 45° shear-SRA curves show a reduced gradient after about 3 s simulation time.

3.3. Set 3: Effect of in situ stress difference

For set 3, five models were simulated with assumed vertical stress of 7, 9, 11, 13 and 15 MPa. Other parameters are listed as follows: (c = 0.6 MPa; φ = 30°; θ = 90°; μ = 1 mPa·s; Q = 0.0035 m^3/s). As the horizontal stress is constant (5 MPa), the corresponding stress differences are 2, 4, 6, 8 and 10 MPa, respectively. As shown in Fig. 8, different HF-joint interaction behaviors were simulated: zero-joint crossing, (for Δσ = 2, 4 and 6 MPa), and 2-joint crossing (for Δσ = 8 and 10 MPa). The simulation results reveal that higher values of in-situ stress difference result in the hydraulic fracture crossing both the upper and lower joints.

As illustrated in the Fig. 9a, the shear-SRA decreases with increase in the stress difference. As the assumed in-situ stress difference is increased from 2 MPa to 8 MPa, the shear-SRA decreases markedly with a reduction in area of 9.35 m^2. The shear-SRA decreases slightly by 1.08 m^2 as the assumed stress difference was increased from 8 MPa to 10 MPa.

Fig. 9b shows the evolution of shear-SRA versus time for different assumed in-situ stress difference. In general, the greater the stress difference, the lower the shear-SRA curve. The initial change in gradient of the of

five curves occurs at about 0.4 s. For models Δσ = 2, 4 and 6 MPa, the cumulative shear-SRA increase with a constant rate. For models with Δσ = 8 MPa and 10 MPa, a significant decrease in shearSRA growth rate can be observed after about 3 s.

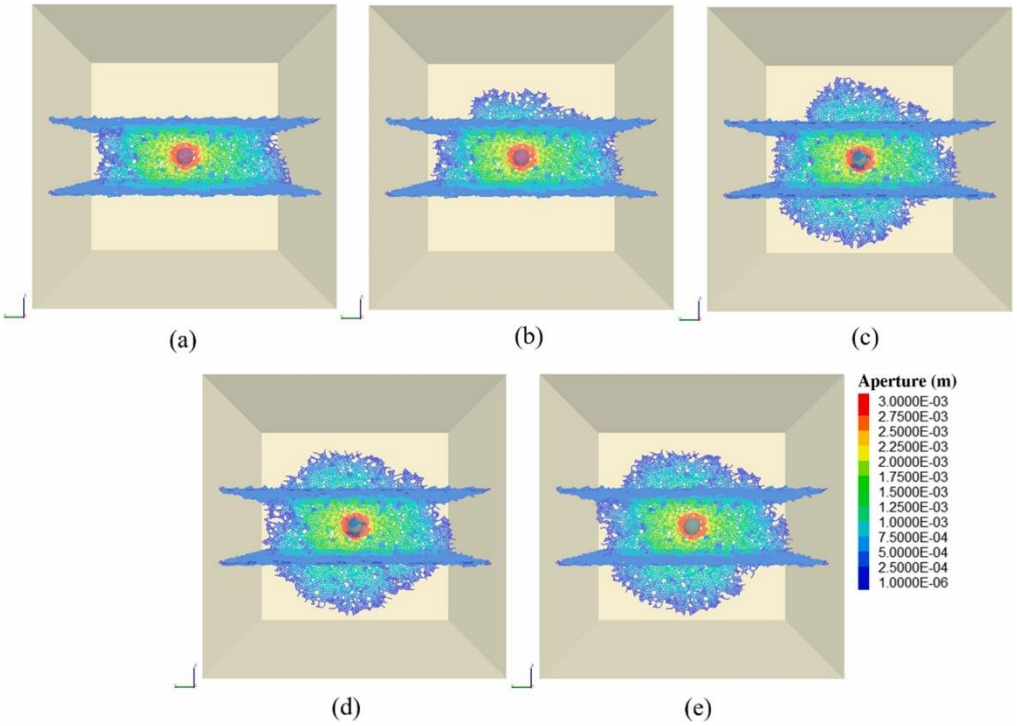

Fig. 4. Interaction between hydraulic fractures and pre-existing joints for different assumed joint cohesion of (a) 0.3 MPa (zero-joint crossing); (b) 0.6 MPa (1-jointcrossing); (c) 0.9 MPa; (d) 1.2 MPa and (e) 1.5 MPa (2-joint crossing).

3.4. Set 4: Effect of approach angle

For set 4, the dip angle of the joints in the five models is assumed at 20°, 15°, 10°, 5°, and 0°. The corresponding approach angle is 70°, 75°, 80°, 85°, and 90°, respectively. Other parameters are listed as follows: (c = 1 MPa; φ = 35°; σ_z = 15 MPa; μ = 1 mPa·s; Q = 0.0035 m^3/s). As shown in Fig. 10, different results were simulated: zero-joint crossing (θ = 70°), 1-joint crossing (θ = 75° and 80°), 2-joint crossing (θ = 85° and 90°). The model simulation results show that higher the approach angles increase the likelihood of the hydraulic fracture crossing the preexisting joint.

As shown in Fig. 11a, the shear-SRA decreases as the approach angle increases. As the assumed approach angle is increased from 70 to 80°, the shear-SRA decreases by 2.75 m^2. The shear-SRA decreased by 1.6 m^2 as the assumed approach angle was increased from 80° to 90°.

Fig. 11b shows the evolution of the shear-SRA versus time for different assumed approach angles. In general, higher approach angles induce a decrease in shear-SRA rates. The shear-SRA increased at a high rate between 0.15 s and 0.4 s, reaching an initial change in gradient at about 0.4 s, and then increasing at a reduced rate until 4.1 s. After 2 s, the shear-SRA rate progressively decrease for increasing approach angles.

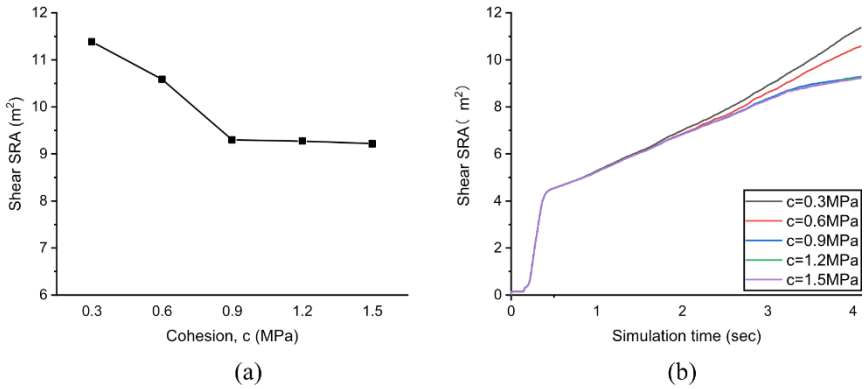

Fig. 5. (a) Shear- stimulated reservoir area, shear-SRA for varying assumed joint cohesion after 4 s simulated fluid injection; (b) Evolution of the shear-SRA with simulation time for varying assumed joint cohesion.

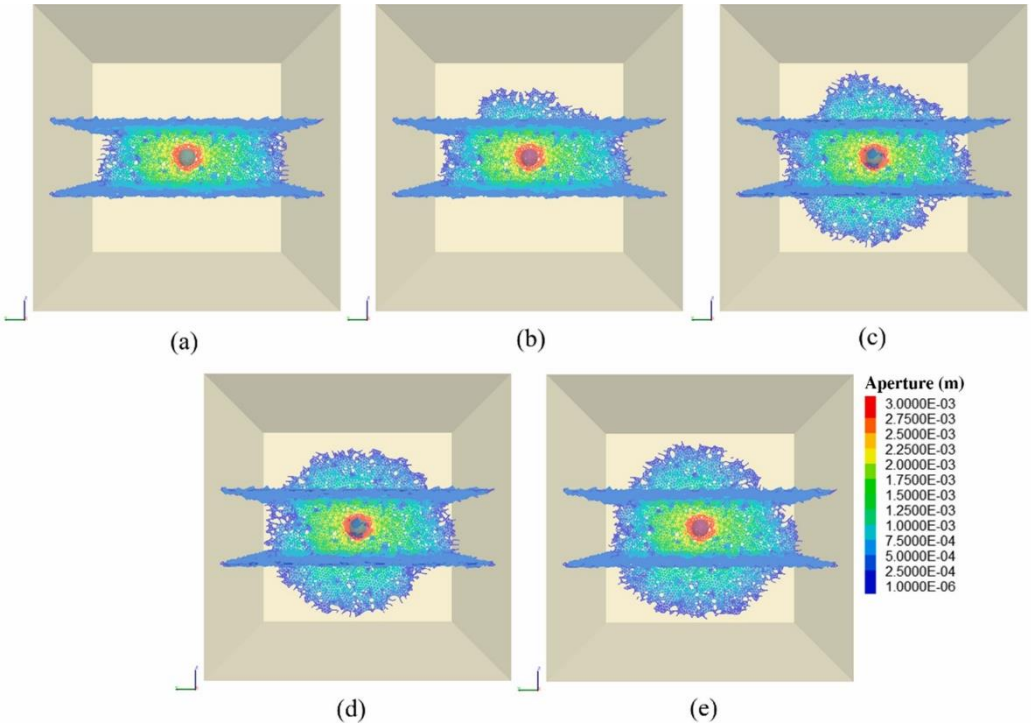

Fig. 6. Interaction between HF and pre-existing joints for varied joint friction angle of (a) 25° (zero-joint crossing); (b) 30° (1-joint crossing); (c) 35° (2-joint crossing);(d) 40° (2-joint crossing) and (e) 45° (2-joint crossing).

3.5. Set 5: Effect of viscosity of treatment fluid

For set 5, five models were simulated assuming varied hydraulic fracturing fluid viscosity of 1, 3, 5, 7, and 9 mPa·s, respectively. Other parameters are listed as follows: (c = 0.6 MPa; φ = 30°; σ_z = 9 MPa; θ = 90°; Q = 0.003 m^3/s). As shown in Fig. 12, different interaction behaviors were observed: zero-joint crossing (μ = 1 and 3 mPa·s), 1joint crossing (μ = 5 mPa·s), 2-joint crossing (μ = 7 and 9 mPa·s). The simulation results indicate that a high value of fluid viscosity is more conducive to the HF crossing joints. Additionally, the radius of the HF decreases with increasing viscosity.

Fig. 13a shows that the shear-SRA decreases with the increase in viscosity. As the assumed viscosity was increase from 1 mPa·s to 5 mPa·s, the shear-SRA decreased from 14.09 m^2 to 9.7 m^2 with a drop of 4.39 m^2.

Conversely, the shear-SRA decreased slightly by 1.24 m^2 as the assumed viscosity was increased from 5 mPa·s to 9 mPa·s.

Fig. 13b shows the evolution of the shear-SRA with time for different assumed viscosity. In general, higher fluid viscosity values cause a decrease in shear-SRA rates, and lower cumulative shear-SRA values. Additionally, the change in gradient of the shear-SRA curves (observed after 0.4 s in previously described model sets) occurs later in the simulation when higher fluid viscosity values are assigned.

Fig. 14 shows the fluid pressure field in the lower joint after 4 s simulated injection time. In order to simplify the distribution of fluid pressure, the value of 9 MPa was arbitrarily chosen (red color indicates that the fluid pressure is greater than 9 MPa). The area of high fluid pressure (shown in red) decreases significantly with an increase in the fluid viscosity from 1 mPa·s to 5 mPa·s. Conversely, the high-pressure area does not vary significantly as the assumed viscosity increases from 5 mPa·s to 9 mPa·s. The simulated variation in the shear-SRA for varied viscosity (Fig. 13a) is in good agreement with the change in the highpressure fluid area within the joint plane.

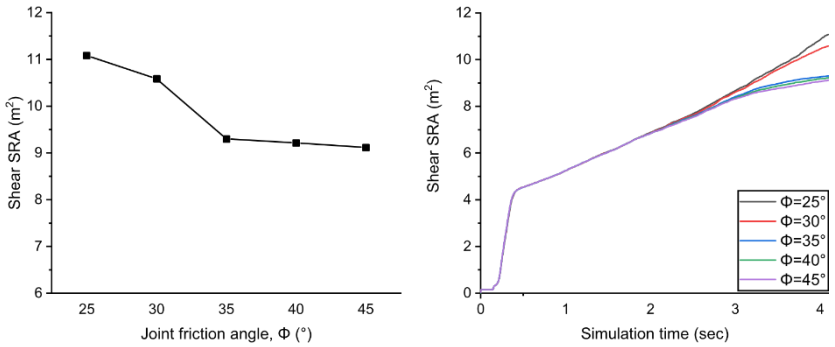

(a) (b)

Fig. 7. (a) Variation of shear-SRA for varied assumed joint friction angle after 4 s injection time; (b) Evolution of the shear-SRA with time for varied assumed joint friction angle.

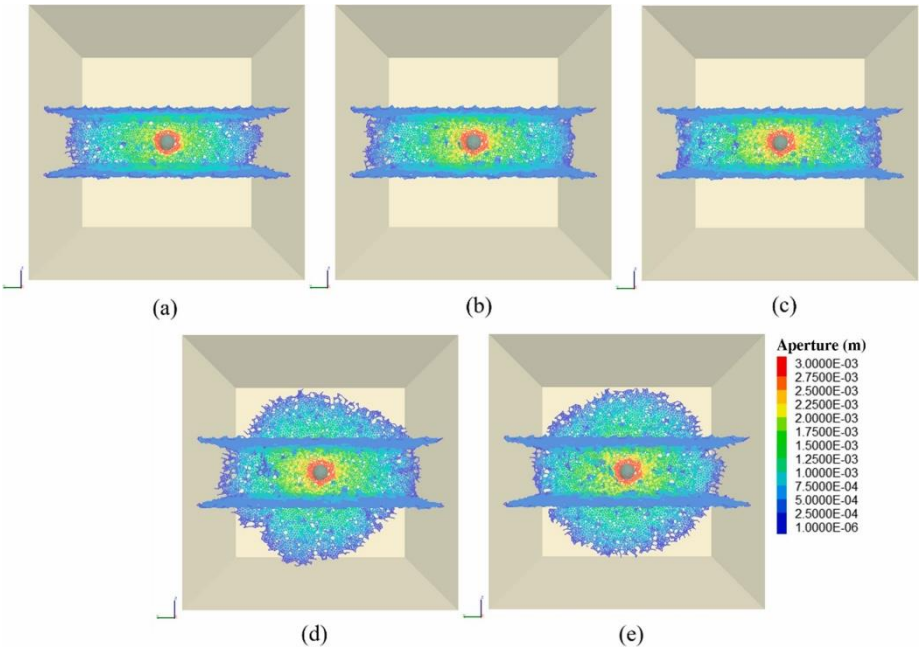

Fig. 8. Interaction between HF and pre-existing joints for varying assumed stress difference (a) 2 MPa (zero-joint crossing); (b) 4MP (zero-joint crossing); (c) 6 MPa (zero-joint crossing); (d) 8 MPa (2-joint crossing) and (e) 10 MPa (2-joint crossing).

3.6. Set 6: Effect of fluid injection rate

For set 6, five models were conducted with assumed injection rates of 0.0025, 0.003, 0.0035, 0.004, and 0.0045 m^3/s, respectively. Other parameters are listed as follows: (c = 0.6 MPa; φ = 30°; σ_z = 12.5 MPa; θ = 90°; μ = 1 mPa·s). As shown in Fig. 15, different results were simulated with respect to the HF-joint crossing relationships: zero-joint crossing, (Q = 0.0025 m^3/s and 0.003 m^3/s), 1-joint crossing (Q = 0.0035 m^3/s), 2-joint crossing (Q = 0.004 m^3/s and
0.0045 m^3/s). The model simulation results indicate that higher values of injection rates are more conducive to HF crossing the pre-existing joints. In addition, the size of the hydraulic fracture increases with increase in injection rate.

As shown in Fig. 16a, there is a steady increase in the shear-SRA between injection rates of 0.0025 m^3/s and 0.0035 m^3/s, followed by a significant decrease in the range 0.035 m^3/s to 0.004 m^3/s, before reaching a limited change for injection rates of 0.004 m^3/s and 0.0045 m^3/s.

Fig. 16b shows the evolution with numerical time of the shear-SRA for different assumed injection rates. For models with assumed values of Q = 0.0025 m^3/s, 0.003 m^3/s, and 0.0035 m^3/s, the shear-SRA-time curves show similar behavior, characterized by a roughly constant shear-SRA rate. These curves can be roughly divided into two stages: a stage of high shear-SAR rate, followed by a stage of reduced rate after 0.4 s simulation time. For models assuming injection rates of 0.004 $m^3/$ s and 0.0045 m^3/s, a significant decrease in the shear-SRA rate occurs after 2.5 s. The shear-SRA of the model with Q = 0.0035 m^3/s after 2.5 s is greater than for models where the assumed Q = 0.004 m^3/s and 0.0045 m^3/s.

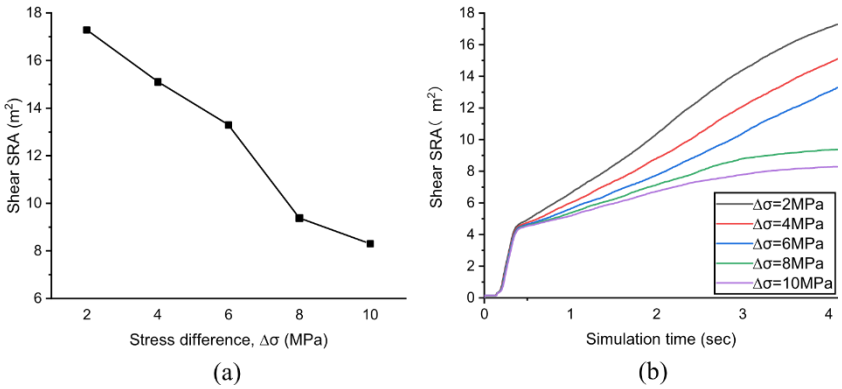

Fig. 9. (a) Variation of shear-SRA for varied assumed magnitudes of in-situ stress difference after 4 s injection; (b) Evolution of shear-SRA with time for varied in-situ stress difference.

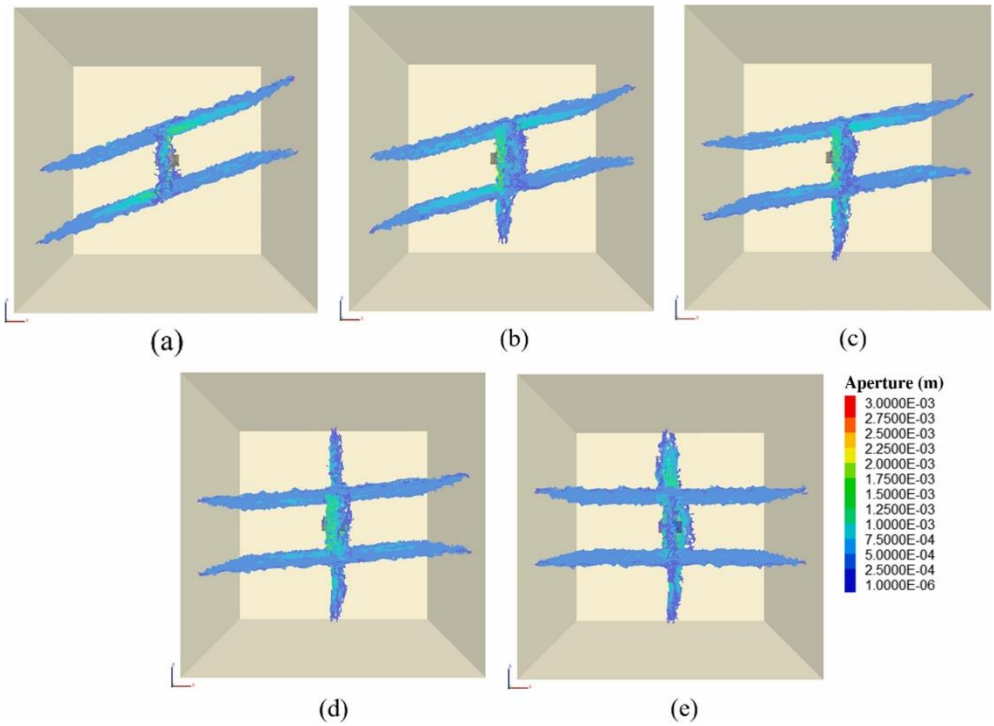

Fig. 10. Interaction between hydraulic fractures and pre-existing joints for varied assumed approach angles (a) 70° (zero-joint crossing); (b) 75° and (c) 80° (1-jointcrossing); (d) 85° (2-joint crossing) and (e) 90° (2-joint crossing).

Fig. 17 shows the fluid pressure field in the lower joint after 3.5 s simulated injection time. With intention to simplify the distribution of fluid pressure, the value of 10 MPa was chosen (red color indicates that the fluid pressure is greater than 10 MPa). The area of high fluid pressure increases with an increase in the fluid injection rate between 0.0025 m^3/s and 0.0035 m^3/s, reaching a maximum area extent for Q = 0035 m^3/s; the high-pressure area then decreases significantly with increased the injection rate from 0.0035 m^3/s to 0.004 m^3/s. Conversely, no significant change in area can be observed between 0.004 m^3/s and 0.0045 m^3/s. The simulated variation in the shear-SRA for different injection rates (see Fig. 16 a) is consistent with the change in the high-pressure fluid field within the joint plane.

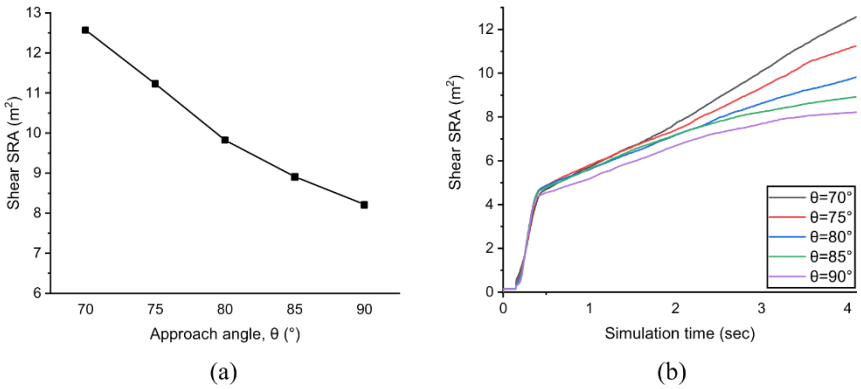

Fig. 11. (a) Variation of the shear-SRA for varied assumed approach angles after 4 s injection; (b) Evolution of the shear- SRA with time for varied assumed approach angles.

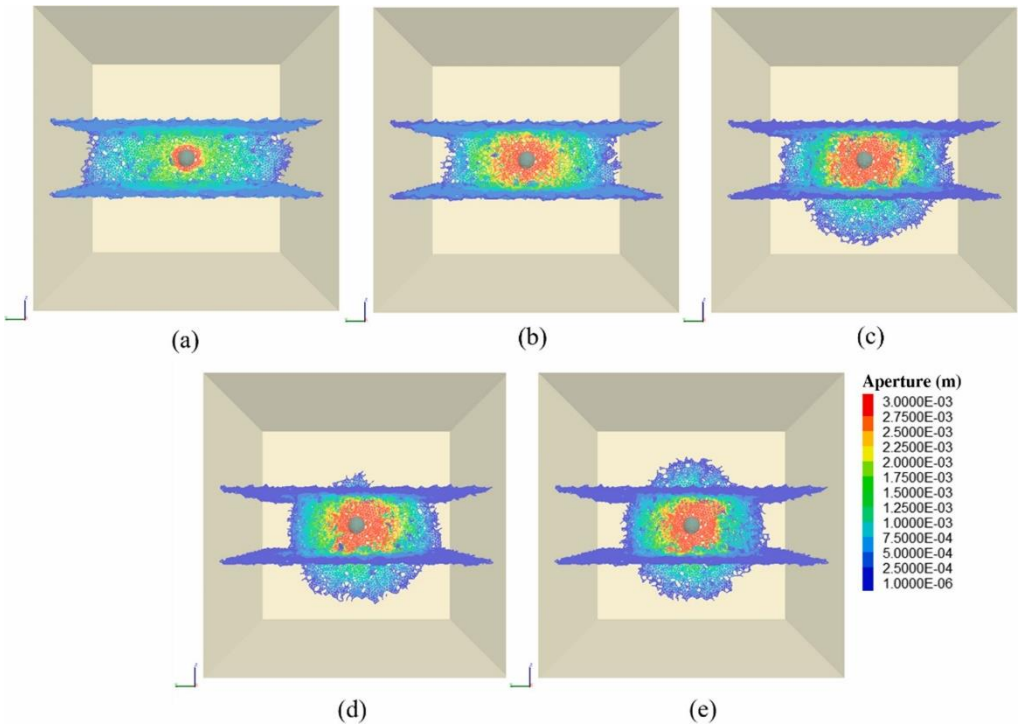

Fig.12. Interaction between hydraulic fractures and pre-existing joints for varied assumed fluid viscosity (a) 1 mPa·s (zero-joint crossing); (b) 3 mPa·s (zero-joint crossing); (c) 5 mPa·s (1-joint crossing); (d) 7 mPa·s and (e) 9 mPa·s (2-joint crossing).

4. Discussion

4.1. Analysis of the factors influencing the interaction between hydraulic fracture and pre-existing joints

The HF-joint interaction mechanism is controlled by multiple factors and physical processes. The occurrence of shear slippage depends on whether the normal stress acting on the pre-existing joint planes yield sufficient shear strength to prevent the planes sliding.

For sets 1 and 2 (varying joint cohesion and friction angle, respectively) an increase of cohesion or friction angle as expected results in an increase in shear resistance. There is a clear inverse relationship between shear-SRA, and joint friction angle and joint cohesion. However, it was found that the value of shear-SRA does not change significantly as the joint cohesion or joint friction angle increases above the threshold values of 0.9 MPa

and 35°, respectively. The simulated shearSRA is less sensitive to further increase of joint cohesion and joint friction angle. As shown in Figs. 6b and 7b, the shear-SRA rate decreases after about 3 s for relatively higher magnitudes of joint cohesion and friction angle cases (2-joint crossing cases). It can be inferred that injection with high-pressure fluid causes some slip of joint, but less slippage would occur after HF cross joint. Hence, there is almost no variation of the value of shear-SRA as the joint cohesion or joint friction angle increases above the threshold values.

The crossing behavior always occur for higher joint cohesion and friction angle cases with smaller value of shear-SRA. As depicted in Fig. 18a, a high stress zone is formed when a bonded interface is considered [51]. High joint strength is conducive to transmit induced stress into the rock on the other side of joint. Therefore, hydraulic fracture tends to cross bonded interface. Sarmadivaleh and Rasouli [18] stated that if the shear strength of an interface is high enough, symmetry of the crack-tip stress field will be maintained, and the propagating fracture will cross the interface. As for frictional interface, no high stress zone was observed on the other side of the joint (Fig. 18b). The intact rock is less likely to be broken and hydraulic fracture pathway may propagate along the frictional interface. Cooke and Underwood [52] stated that crack-tip tensile stresses cannot be transmitted across the interface when slip occurs. We infer that the shear slip of frictional interface reduced the probability of the formation of high stress zone so that the HF tip becomes arrested. In short, the hydraulic fracture tends to cross strong joint, while weak joints are more likely to determine a non-crossing behavior.

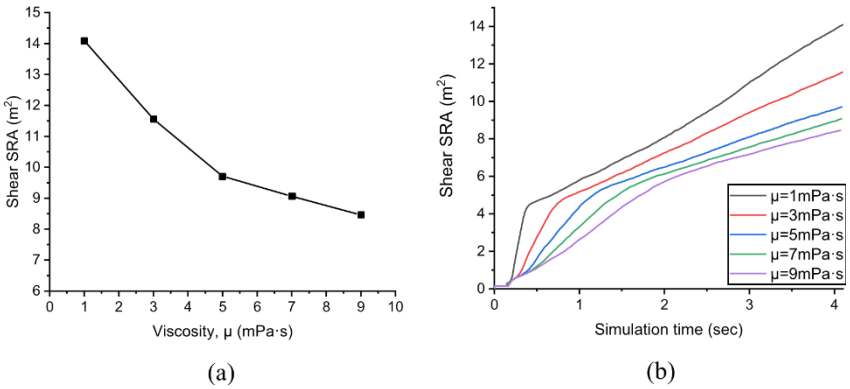

Fig. 13. (a) Variation of shear-SRA for varied assumed fluid viscosity after 4 s injection; (b) Evolution of the shear- SRA with time for varied assumed fluid viscosity.

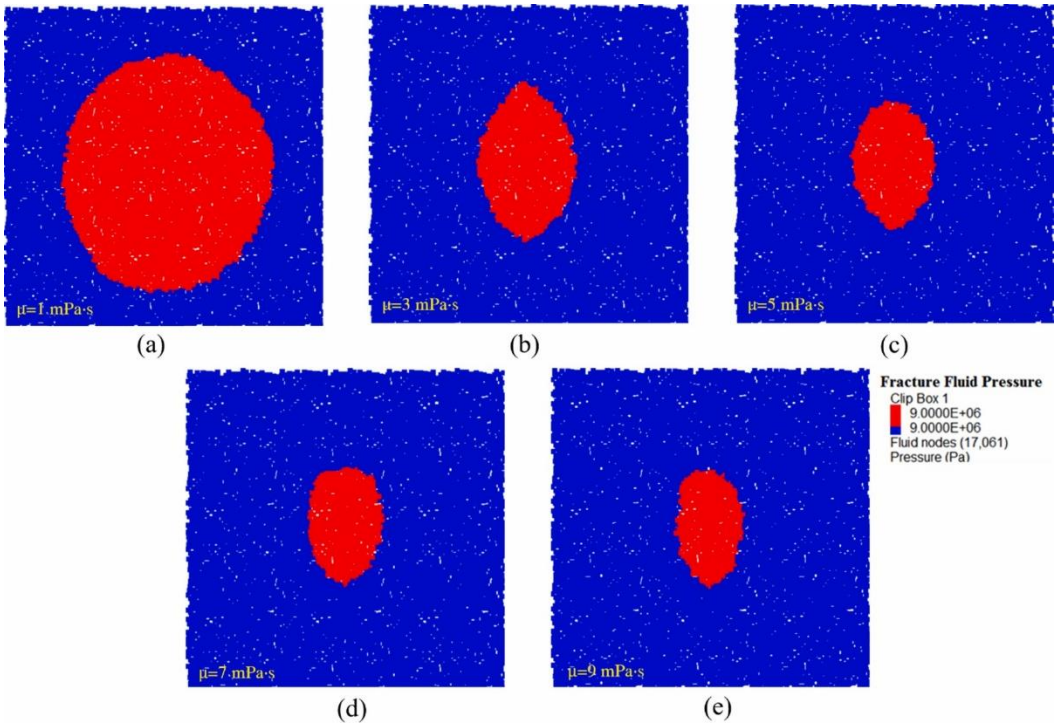

Fig. 14. Fluid pressure field in the lower joint for varied assumed fluid viscosity after 4 s injection (red indicates that fluid pressure exceeds 9 MPa) (a) 1 mPa·s; (b) 3 mPa·s; (c) 5 mPa·s; (d) 7 mPa·s and (e) 9 mPa·s.

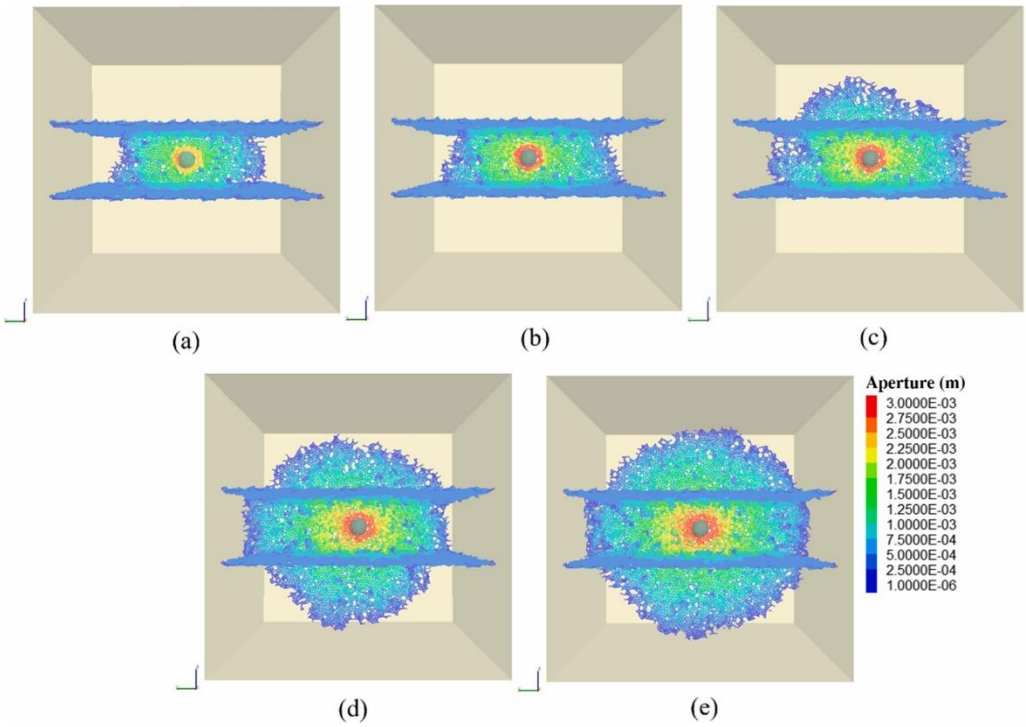

Fig. 15. Interaction between hydraulic fracture and pre-existing joints for varied assumed fluid injection rates (a) 0.0025 m^3/s (zero-joint crossing); (b) 0.003 m^3/s (zero-joint crossing); (c) 0.0035 m^3/s (1-joint crossing); (d) 0.004 m^3/s (2-jont crossing); (e) 0.0045 m^3/s (2-joint crossing).

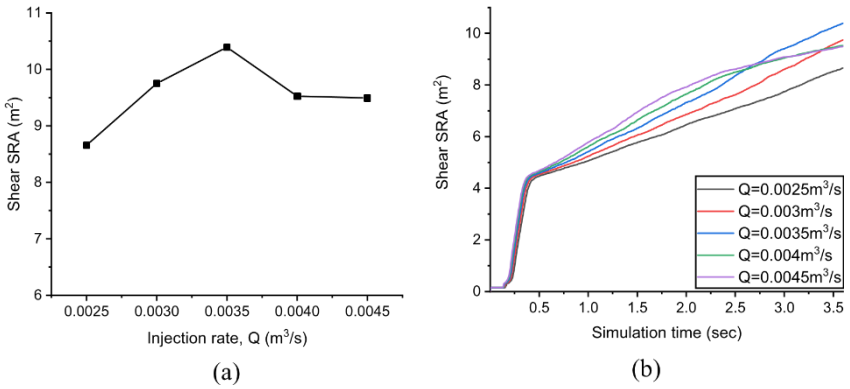

Fig. 16. (a) Variation of shear- SRA for varied assumed fluid injection rates after 3.5 s injection. (b) Evolution of the shear-SRA with time for varied fluid injection rates.

For sets 3 and 4 (varying stress difference and approach angle, respectively), normal stress acting on the joint plane increases as the insitu stress difference and approach angle increases. Hence, the joint planes have an increased resistance to shear slip, resulting in a decrease of shear-SRA rates, thus promoting the formation of a high stress zone on the opposite side of the joint plane [51]. Therefore, higher assumed approach angles and higher stress difference values lead to a greater probability of the hydraulic fracture crossing the pre-existing joints. This observation is in agreement with previous work [8,20].

For set 5 (varying fluid viscosity), the high diffusivity of low- viscosity fluids leads to a larger area of high fluid pressure (Fig. 14). As a result, the shear-SRA in low-viscosity fluid case is much larger than for high-viscosity fluid case. A highly viscous fluid has a higher flow resistance and lower velocity. This can ultimately reduce the penetration of the fluid into the joint, causing a decrease of shear-SRA, compared to simulations using a low-viscosity fluid (Fig. 13a). Injection of high-viscosity fluid induces high fluid pressures surrounding the intersection point, causing a local stress concentration, and leading to greater likelihood of HF propagation on the opposite side of the joint. In brief, the model result indicate that high-viscosity fluid is conducive to the HF crossing the joints, whereas low-viscosity fluids tend to penetrate into the pre-existing discontinuities, which is consistent with laboratory experiments [10,53].

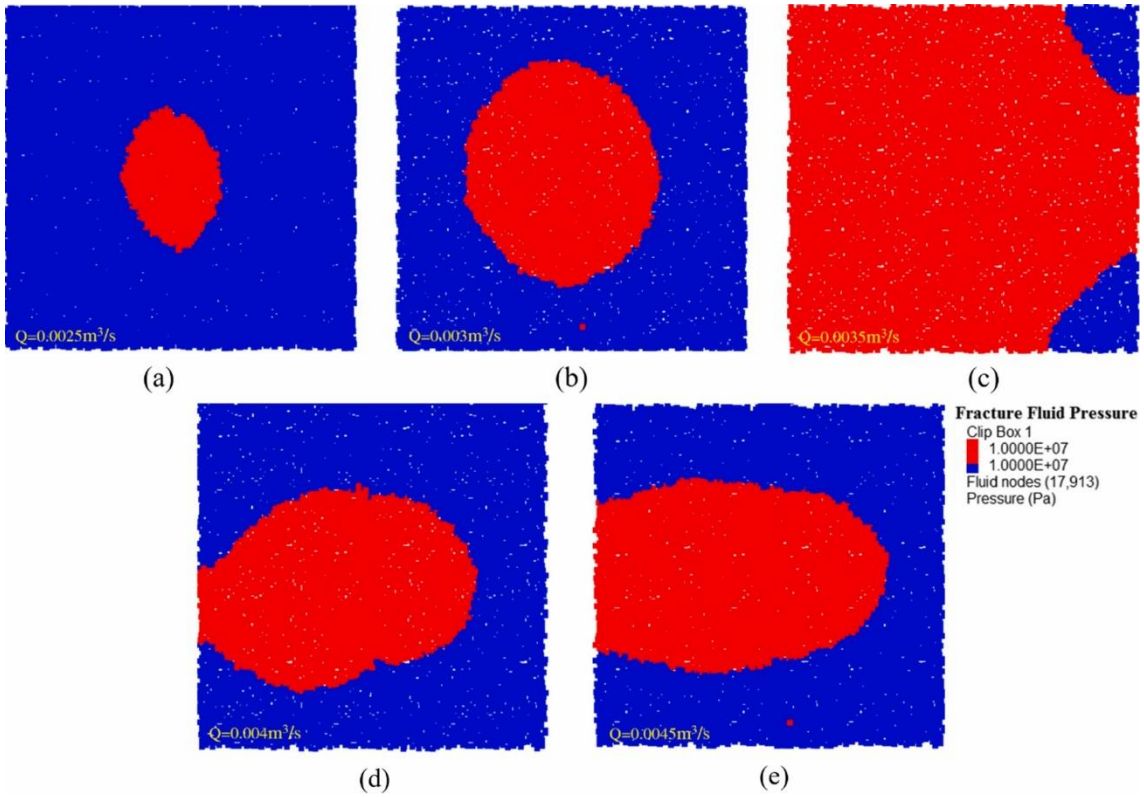

Fig. 17. Fluid pressure field in the lower joint for varied fluid injection rates after 3.5 s injection (red indicates that fluid pressure exceeds10 MPa) (a) 0.0025 m^3/s; (b) 0.003 m^3/s; (c) 0.0035 m^3/s; (d) 0.004 m^3/s; (e) 0.0045 m^3/s.

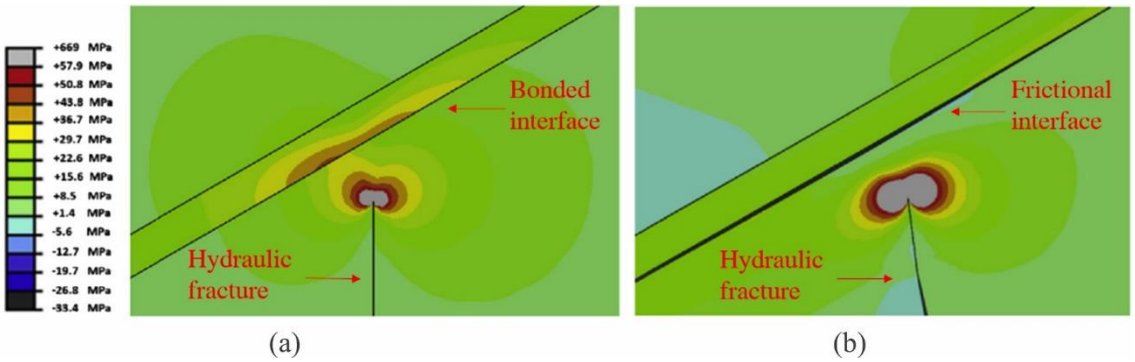

Fig. 18. Maximum principal stress plot for the specimen with (a) bonded interface; (b) frictional interface. After [51].

For set 6 (varying injection rate), we observed that increasing the injection rate (Q = 0.0025 m^3/s to 0.0035 m^3/s) give rise to a larger area of high-pressure in the joint plane, and the shear-SRA reveals a steady increase trend over the range of Q = 0.0025 m^3/s to 0.0035 $m^3/$ s. However, the high-pressure area then decreases significantly with increased the injection rate from 0.0035 m^3/s to 0.004 m^3/s. The main cause of this variation pattern lies in the evolution of crossing behavior. Before the HF crosses the joint, the fluid keep invasion into joint plane, which leads to the fluid pressure in the joint plane increase progressively. After the HF crosses the joint, the injection of fluid mainly acts to dilate/propagate the new induced fracture, and the fluid pressure in the joint plane would not build up sharply. As a result, the area with fluid pressure greater than 10 MPa is the largest in case Q = 0.0035 m^3/s (the lower joint was not cross by HF, see Fig. 15. (c)). For cases Q = 0.004 m^3/s

and 0.0045 m^3/s (2-joint crossing case), no significant change in high-pressure area or shear-SRA can be observed. Besides, the high-pressure area and shear-SRA for cases Q = 0.004 m^3/s and 0.0045 m^3/s are relatively smaller than that for case 0.0035 m^3/s. (more detailed discussion about variation pattern of shear-SRA can be found in Section 4.2).

4.2. Simulated evolution of the hydraulic fracture – joint interaction process

For all 2-joint crossing models (except for set 5, fluid viscosity), it is possible to subdivide the simulated evolution process into five stages. Considering the set 6 with Q = 0.004 m^3/s as an example, Fig. 19a shows the variation of shear-SRA and tensile-SRA for the five stages. The modeled interaction behavior for each stage is also shown in Fig. 20. For all 0-joint-crossing cases, three stages in the evolution process were observed. Considering set 1 with c = 0.3 MPa as an example, Fig. 19b shows the variation of shear-SRA and tensile-SRA for the three stages.

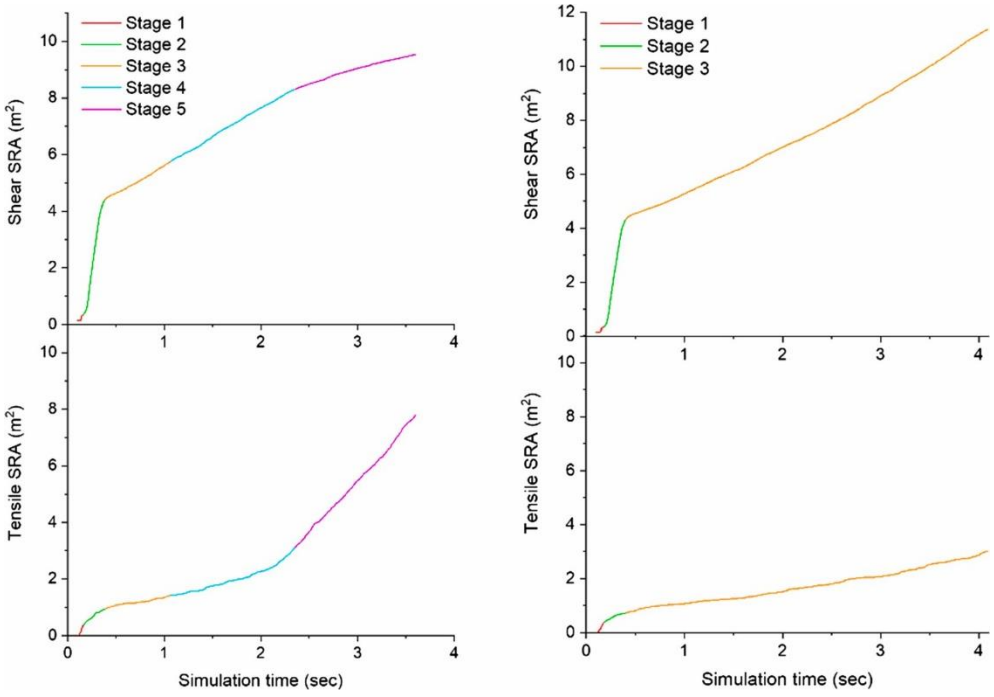

Fig. 19. Variation in the shear-SRA and tensile-SRA at different stages for (a) 2-joint -crossing cases; (b) zero-joint -crossing cases.

Stage 1

As shown in Fig. 20a, a small amount of slip microseismic events occur on the pre-existing joint before the intersection with the hydraulic fracture; these are referred to here as ‘‘dry events’’ [54] (microseismicity generated remotely by poroelastic stress changes). According to Fig. 19 a, the shear-SRA increases by a small amount whereas tensile-SRA undergoes a rapid increase during stage 1. The tensile failure is the main contribution of the flow pathway in stage 1.

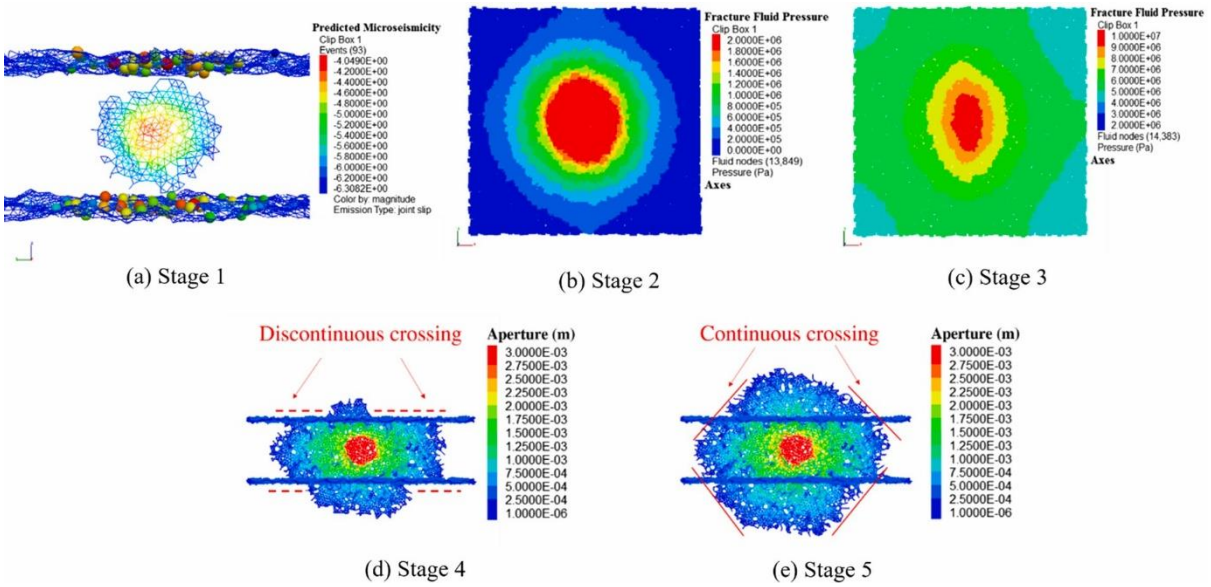

Fig. 20. Hydraulic fracture –joint interaction behavior during different stages for 2-joint -crossing cases.

Gu and Weng [55] suggested that the first step in the hydraulic fracture-joint interaction process is mechanical interaction, where the joint plane is under the influence of the stress induced by HF, but the fluid pressure of the joint plane is considered to remain zero. Highpressure fluid injection in a rock mass causes the initiation and propagation of HF in addition to promoting joint failure in shear. Fig. 21 shows a conceptual diagram where the HF approaches the joint and can be considered as the approach stage of HF-joint interaction [56]. As the tip of the HF approaches the pre-existing joint, the induced stress on the joint becomes progressively higher. Due to the stress perturbation, the shear failure of the joint starts before the HF tip intersect the joint.

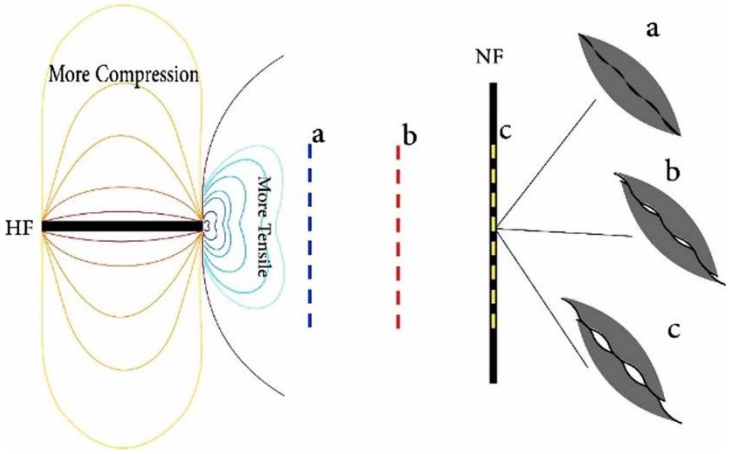

Fig. 21. Hydraulic fracture approaching the pre-existing joint characterized by hydrofrac growth and shear dilation. After [56].

Stage 2

Once the hydraulic fracture intersected the joint, the fluid rapidly penetrates to the edge of the joint from the intersection point. Fig. 20b reveals a radial fluid pressure distribution pattern in the joint, and a fluid pressure gradient from the intersection point towards its edge. The simulated fluid pressure is about 2 MPa around intersection point, while at the edge of the joint is null, indicating the fluid flow is not confined by the edge of

joint. Fluid percolates into the pre-existing joint reducing the effective stress, and in turn the shear resistance is reduced. The changes in effective stress state lead to shear failure on pre-existing joints at fluid pressure below the level required to induce a hydraulic fracture (mode I). This process is referred to as “hydro-shearing” or shear stimulation [57]. Based on our model results, tensile-fracture in intact rock and shear-slip on joints co-exist during all five stages, with a varied ratio of tensile-SRA to shear-SRA. McClure and Horne [3] noted the complex nature of stimulation mechanism in Enhanced Geothermal Systems (EGS). They discussed four conceptual models: pure opening mode (hydraulic fracture), pure shear stimulation (shear slip on preexisting joints), primary fracturing with shear stimulation leak off, and mixed-mechanism stimulation. To maximize the shear failure on preexisting joints rather than tensile-fracture in intact rock, the variations in the ratio of tensile-SRA to shear-SRA during the interaction process should be taken into account. As shown in Fig. 19a, the shear-SRA increases at a high rate in stage 2 whereas the growth rate of the tensileSRA shows a gradual decrease. It can be speculated that the shear failure on joint could be a dominant mechanism controlling HF-joint interaction behavior in stage 2.

Stage 3

With continuous injection, the fluid gradually fills the volume of the joint. After the fluid reaches the edge of the joint, the fluid flow rate within the joint decreases markedly. The increasing fluid pressure within the joint cause deformation in the intact rock and aperture of the joints. As depicted in Fig. 20c, the simulated fluid pressure at the HFjoint intersection point in the considered model is about 10 MPa and over 2 MPa at the joint edge. The continuous increase of fluid pressure keeps reducing the effective normal stress, resulting in additional shear stimulation of pre-existing joints. As the fluid flow become confined by the joint edge (i.e., end of stage 2), the rate of shear stimulation is reduced, together with the area within the joint that remains available for shearing. As a result, shear-SRA rate decreases. At the same time, tensile-SRA slightly increase due to fracturing of intact rock between the two pre-existing joints.

Stage 4

In this stage, the HF crosses the joints, and starts growing. As shown in Fig. 20d, the joint crossing mode is characterized geometrically by a discontinuous crossing pattern, that was also observed by in laboratory experiment [58] (Fig. 22). Given the small volume of new induced fractures, this does not appear to exert a significant effect on the fluid pressure field within the joint. Fluid pressure continues to build up as the fluid injection continues. The shear-SRA rate is constant and moderate, whereas the tensile-SRA rate tends to increase (i.e., the gradient of the curve increases).

As the fluid pressure in the area of the intersection point increases, the stress concentration increases and induces intact rock failure in tension. According to Gu and Weng [55], once the equilibrium between the tensile stress and the rock tensile strength was achieved, a induced fracture would be initiated on the opposite side of the joint plane. Ju [59] also stated that if the forces acting on the joint plane do not cause the shear slippage of joint, the hydraulic fracture tip would be forced to propagate across the joint plane. However, our model results show that both the tensile-SRA and the shear-SRA increase during stage 4, implying tensile-fracture and joint slip co-exist during this stage. Note that Gu and Weng’s criterion does not consider crossing after slip or opening

has occurred, and assumes that fluid percolation of the joint has not started. Laboratory experiment results [24], however, show that the HF can cross the joint even if slip occurred in the joint, and fluid percolated within it. It is clear that both numerical simulation and experiment results indicate that crossing behavior cannot be predicted based exclusively on whether or not slip occur along the joint plane.

Stage 5

As shown in Fig. 20e, in the continuous crossing stage, the edge of the HF is a continuous circular arc. The presence of the joint does not appear to make a significant difference in the shape and orientation of the hydraulic fracture in this stage, as also verified by experimental result [58].

HF always propagates along the preferential fracture plane or the path of least resistance. When it comes to continuous crossing stage, the original fracture plane (the plane normal to minimum principal stress) becomes the easier pathway for fluid flow compared to the joint plane filled with high-pressure fluid. The injection of fluid mainly acts to dilate/propagate the new induced fracture. As a result, no significant shear slippage occurs on the joint plane during stage 5, as evidenced by the distinct reduced rate of increase during stage 5 of the shear-SRA (Fig. 19a). Conversely, a sharp increase is simulated for the tensile-SRA, suggesting that tensile fracture is the main contribution of flow network in stage 5. It should be noted that variation in the fluid viscosity leads to a different pattern of SRA growth (Fig. 13b), and further research is needed to address this behavior.

For 0-joint -crossing cases, as shown in Fig. 19b, three stages of the evolution process were observed. Similar to the first three-stages of the 2-joint-crossing scenarios, the tensile-SRA shows a steeply increasing trend in stage 1. The growth rate of tensile-SRA gradually decreases while the shear-SRA increases sharply in stage 2. Additionally, in stage 3, the tensile-SRA increases at a higher rate than in the previous stages, and the shear-SRA increases at a relatively low rate compared to in stage 2.

There appears to be varying amounts of both tensile-failure in intact rock and shear-failure on pre-existing joints during the evolution process of the HF-joint interaction, controlling dominant pattern of interaction behavior (i.e. joint slip or joint-crossing). This pattern may be due to the fact that fluid flow always follows the path of least resistance (or the direction that minimizes the energy required for the fracture to grow).

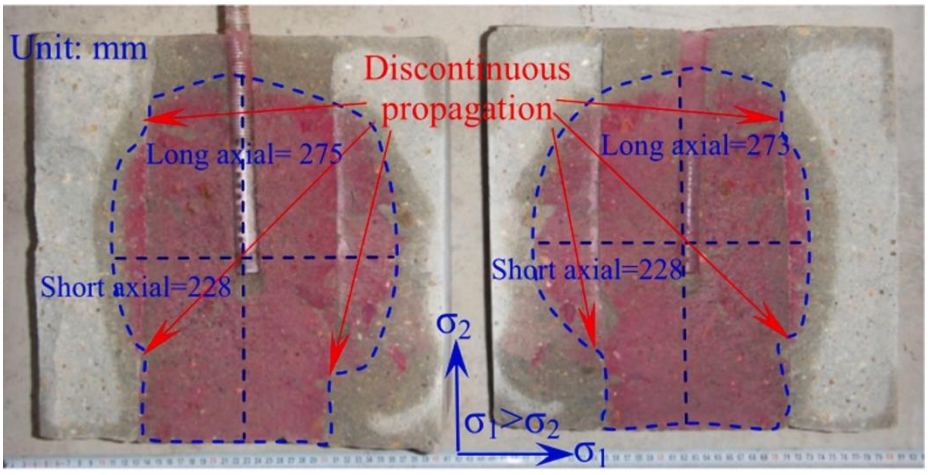

Fig. 22. Discontinuous propagation where HF crossing two pre-existing joints. After [58].

4.3. Modelling challenges and future work

Analyzing the fracture propagation at later times would need larger volumes to be investigated. Therefore, the influence of other joints would become progressively more important. As a result, later stages of HF-joint interaction process would require more complex approaches, such as SRM to include more complex joint networks.

The hydro-mechanical coupling effect is the essential physics of hydraulic fracturing treatment, which required to be accounted for in a robust simulator [60,61]. The XSite numerical modelling code overcomes the disadvantages of over-simplified analytical criteria which are not capable of considering changes in fluid pressure field and the nonlinear-mechanical response of pre-existing joints and intact rock. Even though numerical simulation has made a significant contribution to the understanding the multi-process mechanism of the interaction behaviors, precise prediction of detailed fracture footprint and the stimulated reservoir area remains very challenging, due to parameter uncertainties and spatial variability of pre-existing joints, as well as the heterogeneity of the rock mass, that are difficult to include in numerical modeling unless more complex approaches (e.g., SRM) are employed. Note that numerous numerical methods, such as XFEM, DEM, FDEM, and lattice spring modelling, which all claim to be able to simulate the propagation of cracks. These methods have their own merits and limitations. A comprehensive review of all numerical methods for hydraulic fracturing is out of the scope of this work. A more detailed introduction of numerical methods can be found in the recent review papers [62–64].

Virtual and mixed reality, VR/MR visualisation have been employed to improve interpretation and visualization of dataset in numerical modelling and site characterization [65]. As depicted in Fig. 23, in our recent work, efforts are being made to enhance the interpretation of the 3D trajectory of hydraulic fractures and the changing fluid pressure field using VR/MR techniques, providing an immersive and enhanced engineering experience.

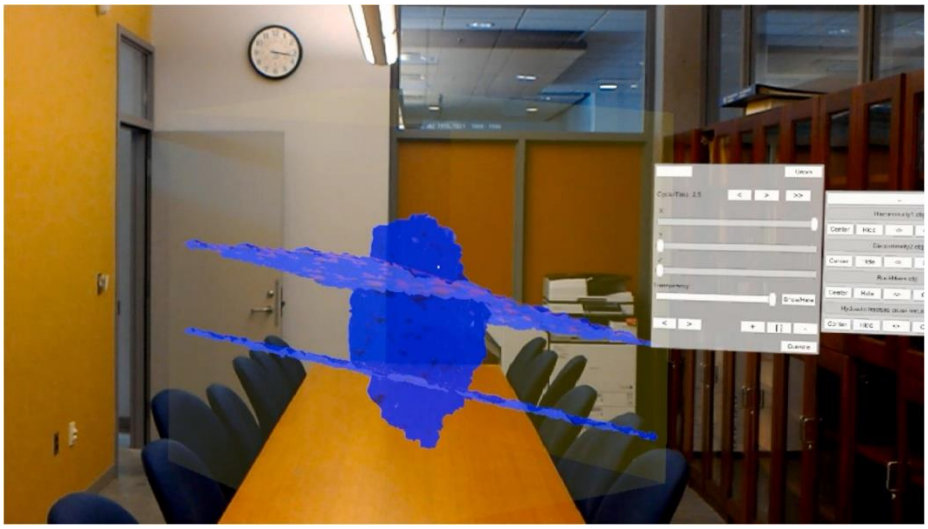

Fig. 23. Hydraulic fracture diagnosis in an interactive MR holographic environment.

5. Conclusions

The 3D hydro-mechanically coupled lattice-spring code, XSite is used to investigate the interaction of hydraulic fractures and pre-existing joints. Six sets simulations were performed to demonstrate the effects of varied joint cohesion, joint friction angle, in-situ stress difference, approach angle, fluid viscosity, and fluid injection rate on the interaction between hydraulic fractures and pre-existing joints. The following conclusions are obtained.

(1) The interactions between hydraulic fractures and pre-existing joints are influenced by multiple factors. XSite model results indicates that high joint cohesion, joint friction angle, in-situ stress difference, approach angle, fluid viscosity, and fluid injection rate are more conducive to hydraulic fractures crossing pre-existing joints. Three basic types of model result were observed: zero-joint crossing, 1-joint crossing and 2-joint crossing. Moreover, whether the HF crosses the joint or not, joint opening and joint slip occur in association with the simulated HF - joint interaction patterns.

(2) The shear-SRA is observed to decrease gradually with increase in joint cohesion, joint friction angle, in-situ stress difference, approach angle and fluid viscosity. Once these input parameters are increased to the high-level values, the simulated shear-SRA is less sensitive to further increases (i.e., 2-joint crossing cases). Additionally, with increase in fluid injection rate, a steady increase in shear-SRA is simulated, followed by a marked decrease, before eventually reaching a stable value. The simulated variation in the shear-SRA is consistent with the change in the high-pressure fluid field within the joint plane.

(3) For the zero-crossing scenario, three stages in the hydraulic fracture-pre-existing fracture interaction and stimulated reservoir area process were observed. The shear-SRA increases slightly whereas tensile-SRA undergoes a rapid increase during stage 1. The shearSRA increases rapidly while the rate of growth of the tensile-SRA gradually decreases in stage 2. The shear-SRA display a constant steady rate of increase during stage 3, whereas a slight increase in the tensile-SRA was observed. The evolution process for the 2-joint crossing models (except for the fluid viscosity models) show two additional stages, stage four (discontinuous crossing pattern) and stage five (continuous crossing pattern), compared to zero-crossing models. There is a markedly slow rate of increase during stage 5 for the shear-SRA, and a rapid increase for the tensile-SRA.

(4) There appears to be both tensile-failure in intact rock and shearfailure on pre-existing joints during the changing process of interaction between HF and pre-existing joints. With different joint mechanical properties, orientation, in-situ stress difference and treatment parameters, the contribution of tensile-failure and shearfailure will be enhanced or reduced, determining the dominant mode of interaction behavior (slip or crossing) in addition to the characteristics of the growth the stimulated reservoir area with simulation time.

We suggest that, in order to maximize the shear-SRA and improve hydraulic fracturing performance in the field, it is necessary to optimize the treatment parameters according to the different mechanical and geological conditions, also considering the evolution of HF-joint interaction process.

CRediT authorship contribution statement

Kaikai Zhao: Writing - original draft, Methodology. **Doug Stead:** Supervision, Project administration, Writing - review & editing. **Hongpu Kang:** Supervision, Funding acquisition. **Branko Damjanac:** Resources, Software. **Davide Donati:** Visualization. **Fuqiang Gao:** Supervision, Investigation, Conceptualization, Writing - review & editing, Funding acquisition.

Declaration of Competing Interest

The authors declare that they have no known competing financial interests or personal relationships that could have appeared to influence the work reported in this paper.

Acknowledgments

This work has been supported by the National Key Research and Development Program of China (grant no. 2017YFC0603003). The first author wishes to thank China Scholarship Council for their support for visiting Simon Fraser University and Itasca Consulting Group, Inc. for providing XSite used for the modeling.

References

[1] Adachi J, Siebrits E, Peirce A, Desroches J. Computer simulation of hydraulic fractures. Int J Rock Mech Min Sci 2007;44:739–57. https://doi.org/10.1016/j. ijrmms.2006.11.006.

[2] Zimmermann G, Reinicke A. Hydraulic stimulation of a deep sandstone reservoir to develop an Enhanced Geothermal System: Laboratory and field experiments. Geothermics 2010;39:70–7. https://doi.org/10.1016/j.geothermics.2009.12.003.

[3] McClure MW, Horne RN. An investigation of stimulation mechanisms in Enhanced Geothermal Systems. Int J Rock Mech Min Sci 2014;72:242–60. https://doi.org/10.
1016/j.ijrmms.2014.07.011.

[4] Kim J, Moridis GJ. Numerical analysis of fracture propagation during hydraulic fracturing operations in shale gas systems. Int J Rock Mech Min Sci 2015;76:127–37. https://doi.org/10.1016/j.ijrmms.2015.02.013.

[5] Yaghoubi A. Hydraulic fracturing modeling using a discrete fracture network in the Barnett Shale. Int J Rock Mech Min Sci 2019;119:98–108. https://doi.org/10.1016/ j.ijrmms.2019.01.015.

[6] Jeffrey RG, Chen Z, Mills KW, Pegg S. Monitoring and measuring hydraulic fracturing growth during preconditioning of a roof rock over a coal longwall panel. ISRM Int. Conf. Eff. Sustain. Hydraul. Fract. 2013 International Society for Rock Mechanics; 2013. p. 893–914. https://doi.org/10.5772/56325.

[7] Kang H, Lv H, Gao F, Meng X, Feng Y. Understanding mechanisms of destressing mining-induced stresses using hydraulic fracturing. Int J Coal Geol 2018;196:19–28. https://doi.org/10.1016/j.coal.2018.06.023.

[8] Blanton TL. An experimental study of interaction between hydraulically induced and pre-existing fractures. Soc Pet Eng – SPE Unconv Gas Recover Symp UGR 1982.
1982. p. 559–62.

[9] Warpinski NR, Schmidt RA, Northrop DA. In-situ Stresses: the predominant influence on hydraulic fracture containment. JPT, J Pet Technol 1982;34:653–64. https://doi.org/10.2118/8932-PA.

[10] Beugelsdijk LJL, De Pater CJ, Sato K. Experimental hydraulic fracture propagation in a multi-fractured medium. Proc. SPE Asia Pacific Conf. Integr. Model. Asset Manag. Society of Petroleum Engineers; 2000. p. 177–84. https://doi.org/10.2523/ 59419-ms.

[11] Zhou J, Chen M, Jin Y, Qing Zhang G. Analysis of fracture propagation behavior and fracture geometry using a tri-axial fracturing system in naturally fractured reservoirs. Int J Rock Mech Min Sci 2008;45:1143–52. https://doi.org/10.1016/j. ijrmms.2008.01.001.

[12] Zhou J, Jin Y, Chen M. Experimental investigation of hydraulic fracturing in random naturally fractured blocks. Int J Rock Mech Min Sci 2010;47:1193–9. https://doi.org/10.1016/j.ijrmms.2010.07.005.

[13] Daneshy AA. Hydraulic fracture propagation in the presence of planes of weakness. Soc Pet Eng – SPE Midwest Oil Gas Ind Symp MGS 1974 1974. https://doi.org/10. 1016/0148-9062(75)91431-x.

[14] Lamont N, Jessen FW. The effects of existing fractures in rocks on the extension of hydraulic fractures. J Pet Technol 1963;15:203–9. https://doi.org/10.2118/419-pa.

[15] Liu Z, Chen M, Zhang G. Analysis of the influence of a natural fracture network on hydraulic fracture propagation in carbonate formations. Rock Mech Rock Eng 2014;47:575–87. https://doi.org/10.1007/s00603-013-0414-7.

[16] Renshaw CE, Pollard DD. An experimentally verified criterion for propagation across unbounded frictional interfaces in brittle, linear elastic materials. Int J Rock Mech Min Sci 1995;32:237–49. https://doi.org/10.1016/0148-9062(94)00037-4.
[17] Gu H, Weng X, Lund J, MacK M, Ganguly U, Suarez-Rivera R. Hydraulic fracture crossing natural fracture at nonorthogonal angles: a criterion and its validation. SPE Prod Oper 2012;27:20–6. https://doi.org/10.2118/139984-PA.
[18] Sarmadivaleh M, Rasouli V. Modified Reinshaw and Pollard criteria for a non-orthogonal cohesive natural interfaceintersected by an induced fracture. Rock Mech Rock Eng 2014;47:2107–15. https://doi.org/10.1007/s00603-013-0509-1.
[19] Blanton TL. Propagation of hydraulically and dynamically induced fractures in naturally fractured reservoirs. Proc. SPE Unconv. Gas Technol. Symp. Society of Petroleum Engineers; 1986. p. 613–21. https://doi.org/10.2523/15261-MS.
[20] Warpinski NR, Teufel LW. Influence of geologic discontinuities on hydraulic fracture propagation. J Pet Technol 1987;39:209–20. https://doi.org/10.2118/ 13224-pa.
[21] Yao Y, Wang W, Keer LM. An energy based analytical method to predict the influence of natural fractures on hydraulic fracture propagation. Eng Fract Mech 2018;189:232–45. https://doi.org/10.1016/j.engfracmech.2017.11.020.
[22] Warpinski N, Kramm RC, Heinze JR, Waltman CK. Comparison of single-and dualarray microseismic mapping techniques in the Barnett Shale. SPE Annu. Tech. Conf. Exhib. Society of Petroleum Engineers; 2005. https://doi.org/10.2118/95568-MS.
[23] Chuprakov D, Melchaeva O, Prioul R. Injection-sensitive mechanics of hydraulic fracture interaction with discontinuities. Rock Mech Rock Eng 2014;47:1625–40. https://doi.org/10.1007/s00603-014-0596-7.
[24] Llanos EM, Jeffrey RG, Hillis R, Zhang X. Hydraulic fracture propagation through an orthogonal discontinuity: A laboratory, analytical and numerical study. Rock Mech Rock Eng 2017;50:2101–18. https://doi.org/10.1007/s00603-017-1213-3.
[25] Zhao Y, He P, Zhang Y, Wang C. A new criterion for a toughness-dominated hydraulic fracture crossing a natural frictional interface. Rock Mech Rock Eng 2019;52:2617–29. https://doi.org/10.1007/s00603-018-1683-y.
[26] Wu K, Olson JE. A simplified three-dimensional displacement discontinuity method for multiple fracture simulations. Int J Fract 2015;193:191–204. https://doi.org/ 10.1007/s10704-015-0023-4.
[27] Kresse O, Weng X, Gu H, Wu R. Numerical modeling of hydraulic fractures interaction in complex naturally fractured formations. Rock Mech Rock Eng 2013;46:555–68. https://doi.org/10.1007/s00603-012-0359-2.
[28] Yamamoto K, Shimamoto T, Sukemura S. Multiple fracture propagation model for a three-dimensional hydraulic fracturing simulator. Int J Geomech 2004;4:46–57. https://doi.org/10.1061/(ASCE)1532-3641(2004)4:1(46).
[29] Dahi-Taleghani A, Olson JE. Numerical modeling of multistranded-hydraulic-fracture propagation: Accounting for the interaction between induced and natural fractures. SPE J 2011;16:575–81. https://doi.org/10.2118/124884-PA.
[30] Guo J, Luo B, Lu C, Lai J, Ren J. Numerical investigation of hydraulic fracture propagation in a layered reservoir using the cohesive zone method. Eng Fract Mech 2017;186:195–207. https://doi.org/10.1016/j.engfracmech.2017.10.013.
[31] Yan C, Jiao YY, Zheng H. A fully coupled three-dimensional hydro-mechanical finite discrete element approach with real porous seepage for simulating 3D hydraulic fracturing. Comput Geotech 2018;96:73–89. https://doi.org/10.1016/j.compgeo. 2017.10.008.
[32] Yan C, Zheng H, Sun G, Ge X. Combined finite-discrete element method for simulation of hydraulic fracturing. Rock Mech Rock Eng 2016;49:1389–410. https://doi. org/10.1007/s00603-015-0816-9.
[33] Yan C, Zheng H. FDEM-flow3D: A 3D hydro-mechanical coupled model considering the pore seepage of rock matrix for simulating three-dimensional hydraulic fracturing. Comput Geotech 2017;81:212–28. https://doi.org/10.1016/j.compgeo. 2016.08.014.
[34] Yan C, Jiao YY. A 2D fully coupled hydro-mechanical finite-discrete element model with real pore seepage for simulating the deformation and fracture of porous medium driven by fluid. Comput Struct 2018;196:311–26. https://doi.org/10. 1016/j.compstruc.2017.10.005.
[35] Cundall PA. A computer model for simulating progressive large-scale movements in blocky rock systems. In: Proc. int. symp. for ISRM, Nancy, Paper II-8; 1971.
[36] Eberhardt E, Stead D, Coggan JS. Numerical analysis of initiation and progressive failure in natural rock slopes-the 1991 Randa rockslide. Int J Rock Mech Min Sci 2004;41:69–87. https://doi.org/10.1016/S1365-1609(03)00076-5.
[37] Kang H, Lou J, Gao F, Yang J, Li J. A physical and numerical investigation of sudden massive roof collapse during longwall coal retreat mining. Int J Coal Geol 2018;188:25–36. https://doi.org/10.1016/j.coal.2018.01.013.
[38] Gao F, Kaiser PK, Stead D, Eberhardt E, Elmo D. Strainburst phenomena and numerical simulation of self-initiated brittle rock failure. Int J Rock Mech Min Sci 2019;116:52–63. https://doi.org/10.1016/j.ijrmms.2019.03.021.
[39] Gao F, Stead D, Coggan J. Evaluation of coal longwall caving characteristics using an innovative UDEC Trigon approach. Comput Geotech 2014;55:448–60. https:// doi.org/10.1016/j.compgeo.2013.09.020.
[40] Nagel NB, Sanchez-Nagel MA, Zhang F, Garcia X, Lee B. Coupled numerical evaluations of the geomechanical interactions between a hydraulic fracture stimulation and a natural fracture system in shale formations. Rock Mech Rock Eng 2013;46:581–609. https://doi.org/10.1007/s00603-013-0391-x.
[41] Mas Ivars D, Pierce ME, Darcel C, Reyes-Montes J, Potyondy DO, Paul Young R, et al. The synthetic rock mass approach for jointed rock mass modelling. Int J Rock Mech Min Sci 2011;48:219–44. https://doi.org/10.1016/j.ijrmms.2010.11.014.

[42] Itasca Consulting Group I. PFC2D (Particle Flow Code in 2 Dimensions) 2008.
[43] Itasca Consulting Group I. PFC3D (Particle Flow Code in 3 Dimensions) 2008.
[44] Damjanac B, Detournay C, Cundall PA. Varun. Three-dimensional numerical model of hydraulic fracturing in fractured rock masses. ISRM Int. Conf. Eff. Sustain. Hydraul. Fract. 2013 International Society for Rock Mechanics; 2013. p. 819–30. https://doi.org/10.5772/56313.
[45] Damjanac B, Cundall P. Application of distinct element methods to simulation of hydraulic fracturing in naturally fractured reservoirs. Comput Geotech 2016;71:283–94. https://doi.org/10.1016/j.compgeo.2015.06.007.
[46] Xing P, Yoshioka K, Adachi J, El-Fayoumi A, Damjanac B, Bunger AP. Lattice simulation of laboratory hydraulic fracture containment in layered reservoirs.
Comput Geotech 2018;100:62–75. https://doi.org/10.1016/j.compgeo.2018.03. 010.
[47] Bakhshi E, Rasouli V, Ghorbani A, Fatehi Marji M. Hydraulic fracture propagation: analytical solutions versus Lattice simulations. J Min Environ 2019;10:451–64. https://doi.org/10.22044/jme.2019.7726.1638.
[48] Fu W, Savitski AA, Damjanac B, Bunger AP. Three-dimensional lattice simulation of hydraulic fracture interaction with natural fractures. Comput Geotech 2019;107:214–34. https://doi.org/10.1016/j.compgeo.2018.11.023.
[49] Damjanac B, Detournay C, Cundall PA. Application of particle and lattice codes to simulation of hydraulic fracturing. Comput Part Mech 2016;3:249–61. https://doi. org/10.1007/s40571-015-0085-0.
[50] Cundall PA. Lattice method for modeling brittle, jointed rock. In: 2nd Int. FLAC/ DEM Symp. Contin. distinct Elem. Numer. Model. geo-mechanics, Melbourne, Australia: 2011.
[51] Wang W, Olson JE, Prodanović M, Schultz RA. Interaction between cemented natural fractures and hydraulic fractures assessed by experiments and numerical simulations. J Pet Sci Eng 2018;167:506–16. https://doi.org/10.1016/j.petrol. 2018.03.095.
[52] Cooke ML, Underwood CA. Fracture termination and step-over at bedding interfaces due to frictional slip and interface opening. J Struct Geol 2001;23:223–38. https://doi.org/10.1016/S0191-8141(00)00092-4.
[53] Zou Y, Zhang S, Ma X, Zhou T, Zeng B. Numerical investigation of hydraulic fracture network propagation in naturally fractured shale formations. J Struct Geol 2016;84:1–13. https://doi.org/10.1016/j.jsg.2016.01.004.
[54] Maxwell SC, Pirayehgar A. Geomechanical Simulation of Different Conceptual Models for Microseismic Interpretation. Proc. 6th Unconv. Resour. Technol. Conf. Tulsa, OK, USA: American Association of Petroleum Geologists; 2018. https://doi. org/10.15530/urtec-2018-2900807.
[55] Gu H, Weng X. Criterion for fractures crossing frictional interfaces at non-orthogonal angles. In: 44th US Rock Mechanics symposium, Salt Lake City, UT, 27–30 June 2010.
[56] Ghaderi A, Taheri-Shakib J, Sharif Nik MA. The distinct element method (DEM) and the extended finite element method (XFEM) application for analysis of interaction between hydraulic and natural fractures. J Pet Sci Eng 2018;171:422–30. https:// doi.org/10.1016/j.petrol.2018.06.083.
[57] Fairhurst C. Fractures and fracturing: Hydraulic fracturing in jointed rock. ISRM Int. Conf. Eff. Sustain. Hydraul. Fract. 2013 International Society for Rock Mechanics; 2013. p. 47–79. https://doi.org/10.5772/56366.
[58] Huang B, Liu J. Experimental investigation of the effect of bedding planes on hydraulic fracturing under true triaxial stress. Rock Mech Rock Eng 2017;50:2627–43. https://doi.org/10.1007/s00603-017-1261-8.
[59] Ju Y, Wang Y, Xu B, Chen J, Yang Y. Numerical analysis of the effects of bedded interfaces on hydraulic fracture propagation in tight multilayered reservoirs considering hydro-mechanical coupling. J Pet Sci Eng 2019;178:356–75. https://doi. org/10.1016/j.petrol.2019.03.049.
[60] Abdollahipour A, Fatehi Marji M, Yarahmadi Bafghi A, Gholamnejad J. A complete formulation of an indirect boundary element method for poroelastic rocks. Comput Geotech 2016;74:15–25. https://doi.org/10.1016/j.compgeo.2015.12.011.
[61] Zhang F, Damjanac B, Maxwell S. Investigating hydraulic fracturing complexity in naturally fractured rock masses using fully coupled multiscale numerical modeling. Rock Mech Rock Eng 2019. https://doi.org/10.1007/s00603-019-01851-3.
[62] Weng X. Modeling of complex hydraulic fractures in naturally fractured formation. J Unconv Oil Gas Resour 2015;9:114–35. https://doi.org/10.1016/j.juogr.2014.07. 001.
[63] Dahi Taleghani A, Gonzalez M, Shojaei A. Overview of numerical models for interactions between hydraulic fractures and natural fractures: Challenges and limitations. Comput Geotech 2016;71:361–8. https://doi.org/10.1016/j.compgeo. 2015.09.009.
[64] Lecampion B, Bunger A, Zhang X. Numerical methods for hydraulic fracture propagation: A review of recent trends. J Nat Gas Sci Eng 2018;49:66–83. https://doi. org/10.1016/j.jngse.2017.10.012.
[65] Onsel IE, Donati D, Stead D, Chang O. Applications of virtual and mixed reality in rock engineering. In: 52nd US Rock Mech Symp 2018. Seattle, WA, USA, 17–20 June 2018.